Layer-by-layer formation of block copolymer derived TiO_2 for solid state dye-sensitized solar cells

Stefan Guldin, Pablo Docampo, Morgan M. Stefik, Gen Kamita, Ulrich Wiesner, Henry J. Snaith, and Ullrich Steiner

Morphology control on the 10-nm length scale in mesoporous TiO_2 films is crucial for the manufacture of high performance dye-sensitized solar cells. While the combination of block-copolymer self-assembly with sol-gel chemistry yields good results for very thin films, the shrinkage during the film manufacture typically prevents the build-up of sufficiently thick layers to enable optimum solar cell operation. Here, we present a study on the temporal evolution of block-copolymer directed mesoporous TiO_2 films during annealing and calcination. The in-situ investigation of the shrinkage process enables the establishment of a simple and fast protocol for the fabrication of thicker films. When used as photoanodes in solid state dye-sensitized solar cells, the mesoporous networks exhibit significantly enhanced transport and collection rates compared to the state-of-the-art nanoparticle based devices. As a consequence of the increased film thickness power conversion efficiencies above 4 % were reached.

1 Introduction

Mesoporosity - porosity on the sub-optical length scale - has become an essential feature in materials design for a wide range of applications, such as dye-sensitized solar cells (DSCs),[1] photocatalysis,[2] electrochemical capacitors,[3] chemical and biochemical sensors,[4,5] and electrochromic devices.[6] The high surface area that is generally necessary in these interface sensitive applications, is conventionally generated by the random close packing of 10-20 nm

S. Guldin, G. Kamita, Prof. U. Steiner
Department of Physics, University of Cambridge,
J. J. Thomson Avenue, Cambridge CB3 0HE, UK
e.-mail: u.steiner@phy.cam.ac.uk

P. Docampo, Dr. H.J. Snaith
Department of Physics, Clarendon Laboratory, University of Oxford, Parks Road, Oxford OX1 3PU, UK

Dr. M. Stefik †, Prof. U. Wiesner
Department of Materials Science & Engineering, Cornell University,
Ithaca, New York 14853, USA
† Now at: Laboratory of Photonic and Interfaces, Institute of Physical Chemistry, École Polytechnique Fédérale de Lausanne, 1015 Lausanne, Switzerland

sized particles, which are obtained by sol-gel chemistry and hydrothermal growth.[7] Although random in pore size and morphological order, these networks have been highly sought-after and boosted research in the field of nanoporous media, in particular for dye-sensitized solar cells.[8] Nevertheless, a random network of sintered nanoparticles lacks detailed control over pore size distribution[7] and exhibits poor charge transport.[9] These limitations have been identified as detrimental for a number of device applications such as the solid state DCSs (ss-DSCs).[10] The replacement of the liquid electrolyte by a solid state hole transporter is motivated by the aim to increase efficiency by reducing the loss in electric potential[11] and to tackle stability and fabrication issues caused by corrosion and leakage of the liquid electrolyte in conventional DSCs.[12] Compared to bulk crystalline anatase TiO_2, the electron mobility in nanoparticle films of TiO_2 is lower by five to six orders of magnitude,[9,13] limiting charge collection and power conversion efficiency in ss-DSCs.[12] The lack of control over the pore size distribution may reduce pore infiltration by the viscous materials required to assemble solid-state devices.[14,15]

New device architectures have been proposed to overcome these limitations, including standing nanowires,[16] fibrous 1-dimensional networks,[17] bicontinuous gyroid networks[18] and block-copolymer directed assembly of sol-gel materials.[19] The latter is particularly promising because it combines detailed control over pore size and morphology on the 10 nm length scale with low-cost and scalable production methods. The structure directing agent in this method is an amphiphilic macromolecule (block-copolymer) which microphase separates into ordered domains on the 5 to 50 nm length-scale driven by the incompatibility of its covalently linked macromolecular blocks. The inorganic material is typically selectively incorporated into one of the polymer domains in form of a nanoparticle sol. The structure-direction by macromolecular self-assembly survives a high-temperature calcination step, resulting in an inorganic material that resembles the polymer microphase morphology. Pioneered by Wiesner and Stucky for silica,[20,21] this concept was soon exploited for nanostructure control in TiO_2.[22–26] In principle, this method should lead to greatly enhanced performance of ss-DSCs, since it allows optimization of the pore size distribution and electron conductivity of the network by varying the molecular weight of the polymer[19] and by controlling the crystallite size within the polycrystalline network,[27] respectively.

Despite these advantages, ss-DSCs based on self-assembled networks still lag behind the best efficiencies of nanoparticle films. A fundamental problem in this manufacture route is the large volume contraction of the block copolymer derived films during the various processing steps. The film shrinkage is induced by the evaporation of residual solvent, the condensation of the inorganic network, the degradation of the polymer, and the crystallization of the TiO_2. As a consequence, films exceeding several hundred nanometers in thickness are subject to crack formation and delamination,[24] which limits the thickness of the photoanode.[28]

Considerable progress has been made in recent years to overcome this fundamental issue. Carbone and coworkers proposed a sequential coating and step-by-step calcination to release stresses during the stack build-up.[29] Unfortunately the removal of the polymer during each

calcination step caused a densification of the underlying layers with each subsequent coating. Grosso and coworkers improved this approach by altering the dip coating technique and protecting the pores after each deposition cycle with a sacrificial polymer to maintain the mesoporosity throughout the structure.[30] The group of Li reported the fabrication of several µm thick mesoporous films by the introduction of a synthesis procedure which is based on the deposition of an already gelled solution, followed by a post-deposition treatment in silicone oil.[31] Other approaches include the incorporation of nanoparticles to prevent the formation of microcracks[32,33] and multilayer deposition combined with a sequential rapid calcination process[34] to reach thicker films. One appealing concept to reach thicker films is to decouple the material manufacturing from the film fabrication by synthesizing and crystallizing the mesoporous TiO_2 in the bulk. The as-made material is then processed into a paste and deposited onto a substrate following established routes for nanoparticle-based DSCs. Thick films for highly efficient liquid electrolyte DSCs have been reported,[35] but the initial self-assembled morphology does not seem to be reflected in the final mesoporous film.[36] Most previous approaches to thick block copolymer-directed films have been applied to liquid electrolyte DSCs, where demands on a fully continuous and highly conducting TiO_2 network are somewhat less crucial, due to extremely long electron diffusion lengths. Apart from reference[36] the material routes for thick mesoporous films are based on the commercially available Pluronic polymer system (poly(ethylene oxide-*b*-propylene oxide-*b*-ethylene oxide). As a consequence of its low molecular weight, pores sizes are below 10 nm and the limited wall thickness does not facilitate complete crystallization while preserving the mesostructure. Limitations in pore diameter, crystallinity, and crystal sizes make this system less ideal for ss-DSCs.

This study is motivated by the aim to establish a simple, straight-forward protocol for the assembly of thick mesoporous films from high molecular weight block-copolymers and their subsequent implementation in ss-DSCs. We present a study of the temporal evolution of polymer directed TiO_2 films during annealing and calcination. The in-situ investigation of the shrinkage process has enabled us to identify a suitable processing window for a simple and fast treatment protocol which promotes the formation of thick mesoporous bicontinuous films with sufficiently large pores. When used as photoanodes in ss-DSCs the mesoporous networks exhibit significantly enhanced transport and collection rates, as compared to the state-of-the-art nanoparticle films. As a consequence of the increased film thickness the manufactured ss-DSCs reach power conversion efficiencies of over 4 %.

2 Results and discussion

The necessity of a stepwise release of stresses in a layer-by-layer approach becomes clear when investigating the loss in film thickness of an initially 700 nm thick layer as a function of temperature. Figure 1a shows the shrinkage of films exposed overnight to temperatures between 50 °C and 600 °C. Film shrinkage levels off at around 400 °C, after evaporation of residual solvent, condensation of the TiO_2 network and complete oxidation of the polymer have led to a decrease in film thickness of 60 %. Earlier work has shown, that in a layer-by-

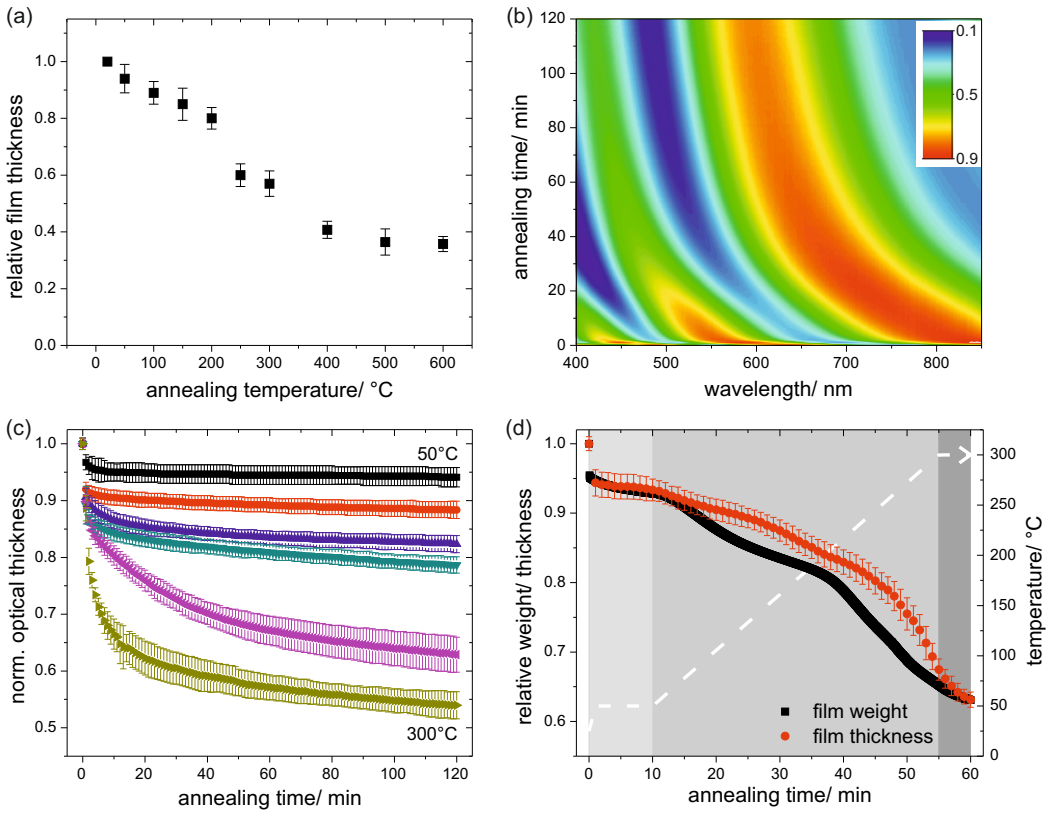

Figure 1. Monitoring of the hybrid film shrinkage process. (a) Ex-situ development of film thickness d as a function of the annealing temperature, determined by ellipsometry and profilometry. Films were annealed overnight at each temperature. (b) Optical response of a hybrid film during annealing at a temperature of 250 °C, illustrated in a contour plot. The reflection intensity, normalized to that of a bare silicon wafer is represented in a multi-color scheme. The shrinkage of the films corresponds to a shift of the reflectance maxima and minima to smaller wavelengths. Each reflectance spectrum was correlated to an optical film thickness by least square fitting. (c) Development of the optical film thickness with time for different annealing temperatures (from top to bottom: 50 °C - 300 °C in 50 °C steps). Error bars shown include fitting uncertainties as well as statistical standard deviation derived from 3-5 runs. Results from ex-situ (a) and in-situ (b, c, Supporting Information) measurements led to the establishment of an annealing protocol which consists of 10 min at 50 °C followed by a linear 45 min heat ramp to 300 °C and a final dwell time at 300 °C for 5 min. (d) Development of the optical film thickness of layers subject to the proposed annealing protocol (●). In contrast to annealing at a fixed temperature, shrinkage occurs gradually, leading to a thickness reduction by 37 % (statistical average of 5 runs). For comparison the weight loss of the films (■) was derived by thermogravimetric analysis (TGA) under the identical heating procedure. The temperature profile is shown as a white dashed line.

layer approach a step-wise calcination of the hybrid films leads to the filling of the underlying pores and therefore densification the inorganic network with each following layer.[29] On the other hand, we have shown that the organic material in the PI-b-PEO/TiO_2 hybrid system is exceptionally resistant to annealing temperatures up to 300 °C. When comparing the TGA results of a hybrid sample to the data of the purely organic and inorganic materials, we found that the weight loss is significantly retarded to higher temperatures, which is attributed to the fact that the TiO_2 sol complexes with the PEO to form a hybrid matrix, making the organic component less susceptible to oxidation.[37] The organic material that remains at 300 °C is essential for a layer-by-layer stacking since this sacrificial material protects the pores of the underlying film during the deposition of the following layer. On the other hand, the condensation of the inorganic network is more or less complete at 300 °C, preventing the partial dissolution of the underlying network in contact with the spin-coating solution during the cyclical film deposition process. In the layer-by-layer technique presented here, we therefore anneal each layer up to 300 °C, which maximises layer contraction (and thereby stress relaxation), while maintaining pore-protecting organic material within the inorganic matrix. Following a similar route, we have recently shown that subsequent layers in a multilayer stack are identical in their optical properties, i.e. of similar porosity and film thickness.[37] This is convincing evidence that in contrast to earlier approaches,[29] the pore size and pore shape stays constant throughout the layers.

In order to resolve the kinetics of the shrinkage process, we monitored the annealing of the films in-situ on a hotplate by collecting their reflection spectra. A contour plot of a time resolved reflection spectrum for an annealing temperature of 250 °C is shown in Figure 1b. The position of the interference fringes depend on the effective refractive index of the material (n) and the thickness of the film (d). A shift of the reflectance maxima and minima to smaller wavelengths corresponds to a reduction of the optical thickness of the films. From the reflection spectra we obtained the optical film thickness ($n \cdot d$) by least square fitting. Complementary ex-situ measurements of the individual development of n for individual temperature steps are shown in the Supporting Information. These results suggest that n is much less affected by the temperature annealing, with a maximum decrease by $\approx 6\%$ after annealing at 300 °C overnight. Figure 1c shows the time resolved evolution of the optical film thickness. 3-5 runs were carried out at temperatures between 50 °C and 300 °C in 50 °C steps (see Supporting Information for raw data). These results enabled us to establish an annealing protocol, which enables the gradual decrease of thickness with time and temperature, but limits the processing time to a minimum. Our protocol consists of an initial 10 min dwell time at 50 °C to evaporate the solvent and promote microphase separation, followed by a linear 45 min increase in temperature to 300 °C, where the films remain for 5 min before they are rapidly cooled down. In comparison to static annealing at a fixed temperature (Figure 1a-c), the temperature protocol has the beneficial effect of slowly and gradually reducing the film thickness to 63 % (Figure 1d). The greatly enhanced film integrity is a direct consequence of this annealing protocol. A complementary measurement of the weight loss of the films subject to this temperature procedure is shown

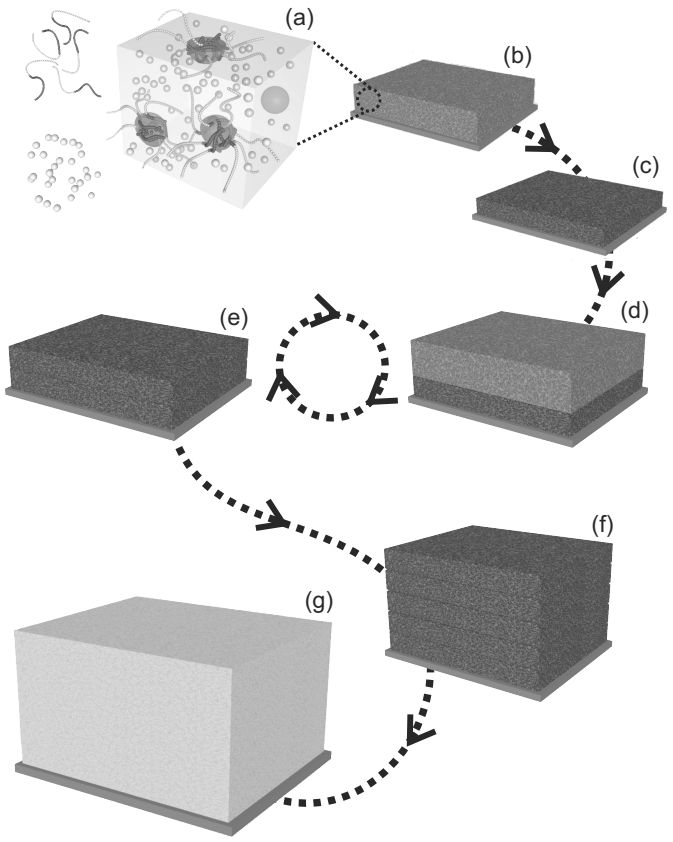

Figure 2. Schematic of film fabrication. (a) A solution of PI-*b*-PEO copolymer and TiO_2 sol is co-deposited on a FTO-covered glass substrate by spin-coating, doctor blading, or dip-coating. The inorganic component preferentially resides in the poly(ethylene-oxide) phase and is therefore structure-directed during the self-assembly process of the amphiphilic block copolymer. (b) After deposition from solution, the film contains residual solvent and the inorganic material has not yet fully condensed into a titania network. The hybrid film is then subjected to a 60 min temperature ramp to 300 °C, which leads to a thickness shrinkage of $\sim 45\%$ (c). Film deposition and heating are repeated several times (d, e) to reach the desired overall film thickness (f). Final high temperature annealing at 600 °C removes the organic components and crystallizes the TiO_2 film (g).

for comparison. After 60 min annealing to 300 °C, the films retain 63 % of their initial weight. This compares to a weight of 33 % after removing the residual organic material and crystallizing the TiO_2 network at 500 °C, confirming that a significant amount of organic material is still present at 300 °C, protecting the pores during successive layer deposition.

Figure 2 illustrates the sample preparation route which is based on this principle. Poly(isoprene-*block*-ethylene oxide) (PI-*b*-PEO) was dissolved in an azeotrope mixture of toluene and 1-butanol. A TiO_2 sol was prepared separately by the hydrolysis of titanium isopropoxide in an aqueous environment and subsequently added to the polymer solution in an inorganic to organic weight ratio of 1. The hybrid solution was then deposited onto an FTO substrate by spin coating or doctorblading to fabricate a dry film of ~ 700 nm in thickness. Upon evaporation of the solvent, the hybrid material phase separates into nm-sized domains, where the TiO_2 sol resides in the hydrophilic PEO block to form a matrix which surrounds the pore forming hydrophobic PI block. The use of an azeotrope with a common high boiling point promotes a slow and even evaporation of hydrophobic and hydrophilic solution components. Significant release of the stresses, associated with the film

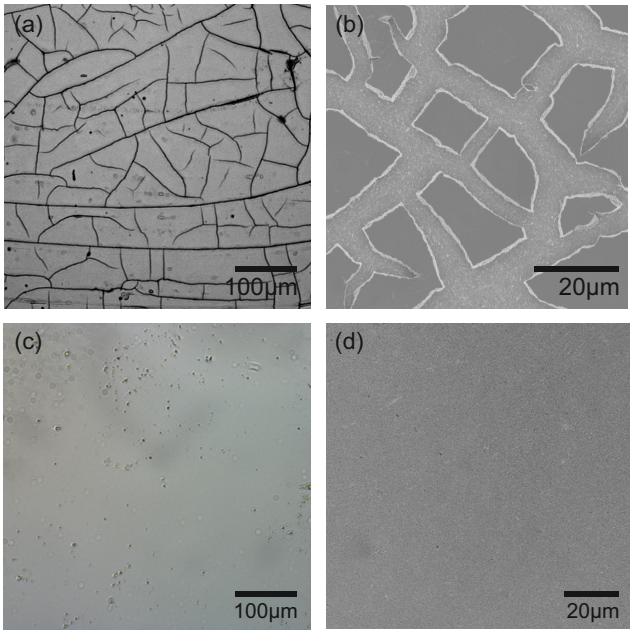

Figure 3. Film quality and cracking behavior. (a,b) Processing of an initially 2.5 µm thick film that was deposited in one single step. Evaporation of solvents leads to the formation of cracks even at room temperature, as seen by transmission optical microscopy (a). These initial cracks grow during calcination and TiO_2 crystallization, leaving large substrate areas uncovered ($> 40\%$), shown by SEM in (b). (c-d) Formation of a similarly thick film in 6 cycles. (c) Optical micrograph of the hybrid film before and (d) SEM image of the 2.5 µm thick film after calcination and TiO_2 crystallization.

shrinkage upon annealing and calcination (Figure 1) is achieved by exposing the film to a temperature protocol of 10 min at 50 °C, followed by a 45 min linear heating ramp to 300 °C and a final dwell time of 5 min at this temperature. A stack is produced by repeating the film deposition and annealing cycles to reach the desired final film thickness in typically 3-7 steps. Finally, a high temperature step at 600 °C for 3 h removes the organic components and crystallizes the TiO_2 . See experimental section for further details.

This protocol enabled us to stack up the film in a layer-by-layer fashion, releasing most of the stresses caused by volume reduction before subsequent layer deposition. The benefit of this protocol is shown in Figure 3, where a 2.5 µm thick stack consisting of 6 layers is compared to a 2.5 µm thick film made in a single step. Figure 3a shows a transmission optical micrograph shortly after the deposition of a highly concentrated solution to form a 2.5 µm thick film. The evaporation of solvents has led to the formation of cracks even before temperature annealing. After annealing, calcination and TiO_2 crystallization at high temperatures, the film has broken up into isolated islands of mesoporous TiO_2 shown in the scanning electron micrograph in Figure 3b, uncovering a large substrate area ($> 40\%$). In contrast, an equally thick film deposited in 6 cycles shows no cracks before (Figure 3c) and after (Figure 3d) annealing at 600 °C.

The use of the PI-*b*-PEO block-copolymer is particularly attractive because the combination of a high PI-PEO Flory-Huggins interaction parameter with low glass transition temperatures of both blocks and the large degree of polymerization results in a much more robust and fast phase separation as compared to the Pluronic system.[38] Rather than time

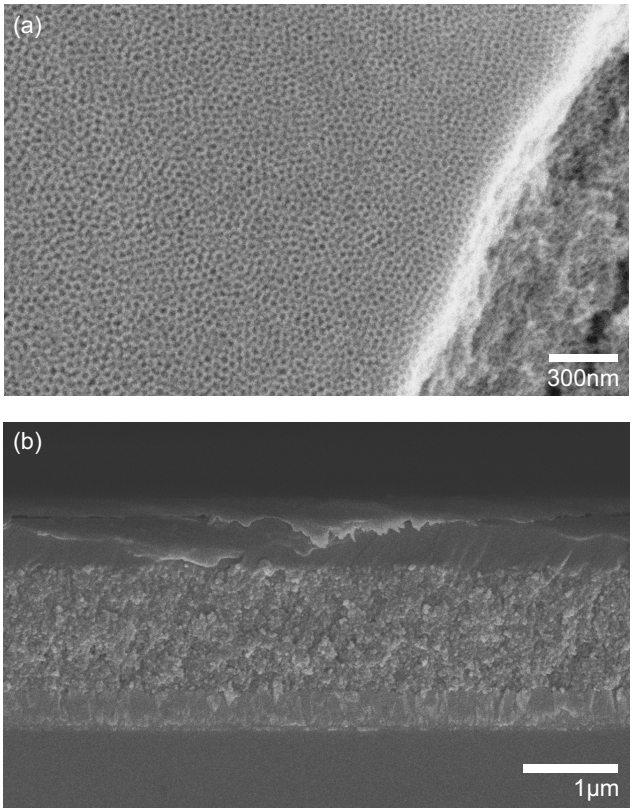

Figure 4. Electron micrographs of the microphase morphology. (a) SEM top-view of a 1.3 µm thick mesoporous TiO_2 film, assembled in 4 deposition and annealing cycles. The pores arising from block copolymer assembly are fully accessible and no overlayer has formed. (b) Cross-sectional SEM image of a fully assembled ss-DSC, where the network has been infiltrated with the hole conducting Spiro-OMeTAD.

consuming protocols, the PI-*b*-PEO microphase morphology forms within minutes, allowing fast and reliable multilayer assembly. The relatively high degree of polymerization of the hydrophobic PI block enables the formation of a network of large pores, facilitating the infiltration of macromolecular compounds. We have previously shown that it is possible to finely tune the pore size of the mesoporous network between 15 and 80 nm, depending on the molecular weight of the sacrificial polyisoprene block and the mixing ratio between polymer and inorganic sol in the initial solution.[19,36] This compares to a very heterogeneous pore size distribution in standard nanoparticle-based photoelectrodes, where the pores are generated by the random dense packing of spheres.[7] The pores in block copolymer-derived photoelectrodes are highly interconnected and highly accessible via infiltration.[37] Furthermore, we have recently shown that subsequent layers in a multilayer stack are identical in their optical properties, i.e. of similar porosity and film thickness.[37] This is convincing evidence that, in contrast to earlier approaches,[29] the pores are fully protected during the deposition process, which means that the pore size and pore shape after calcination are constant throughout the layers.

The morphology of a TiO_2 photoanode fabricated by 4 deposition and annealing cycles and a final high temperature step is shown in Figure 4. Pores are well discernible on the top surface of the 1.3 µm thick stack, indicating that the pore-network is fully accessible

from the top. No solid TiO_2 overlayer has formed which could impede the infiltration of the network. Figure 4b shows the cross-section of a fully assembled ss-DSC, after dye sensitization and infiltration of the network with the hole conductor spiro-OMeTAD.

Thick porous multilayer photoanodes assembled into ss-DSCs exhibit remarkable photovoltaic performance. Figure 5a shows the current-voltage characteristics of the best performing device, with a short circuit current (J_{sc}) of 8.0 mA cm^{-2}, an open-circuit potential (V_{oc}) of 0.81 V and a fill factor (FF) of 0.63, resulting in a power conversion efficiency (η) of 4.0 % using the organic dye CN04.[39] This is a significant improvement over previously reported efficiencies of block copolymer assembled ss-DSCs, with best efficiencies of $\eta = 2.5\%$[27] and $\eta = 1.5\%$.[19] In both cases, attainable film thicknesses were limited by cracking and delamination, resulting in insufficient light absorption in the manufactured devices. Devices were also created using the indolene based organic dye D102, which is often used to create reliable ss-DSCs. Figure 5b shows the best working devices based on this dye, comparing the block copolymer (BCP) assembled and conventional TiO_2 nanoparticle (NP) systems, both reaching similar power conversion efficiencies of $\approx 3.6\%$. While the NP system has a higher value of J_{sc}, The BCP multilayer devices excel in the open-circuit voltage and fill factor. Figure 5c and d show an overview of the key photovoltaic device parameters J_{sc}, η, V_{oc}, and FF as a function of the film thickness of the BCP-assembled photoanode (data from 12 devices were averaged for each thickness). A reasonably constant performance was observed for photoanode thicknesses between 1.3 and 2.0 µm. A

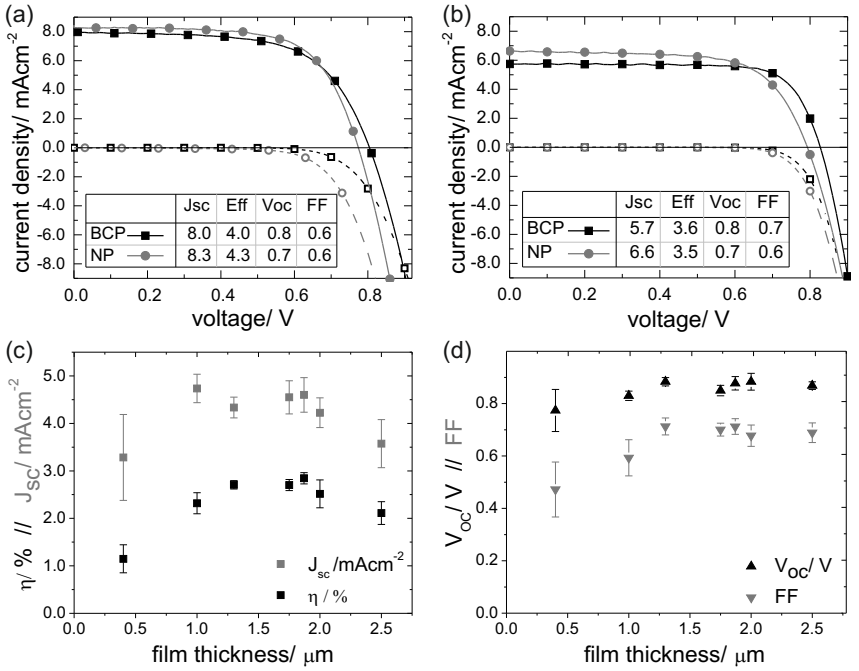

Figure 5. Photovoltaic device performance. (a) Current-voltage characteristics of the highest efficiency ss-DSCs based on a 1.3 µm thick BCP-derived photoanode (■) compared to a NP-assembly (●). The CN04[39] dye was used in both devices. The filled symbols correspond to a simulated AM 1.5 full sun light illumination (100 mW cm^{-2}), the open symbols to the dark current. (b) Current-voltage curves of similar devices based on the D102 dye. (c, d) Key photovoltaic device parameters as a function of the thickness of the active layer. (c) Short circuit current (J_{sc}, ●), and power conversion efficiency (η, ■) of BCP-assembled devices. (d) Open-circuit voltage (V_{oc}, ▲), and fill factor (FF, ▼).

photoanode thickness of 2.5 µm resulted in a significantly lower J_{sc}, whereas $V_{oc} \approx 0.87\,V$ and $FF \approx 0.7$ are retained for this thickness.

Block copolymer assembled photoanodes have been previously reported to exhibit faster electron transport compared to random nanoparticle networks.[27] In Figure 6 we show the charge recombination, transport and collection rate as a function of the applied bias for multilayer BCP photoanodes, compared to devices incorporating standard NP films of the same thickness. From Figure 6a, it is evident that charge transport in a 5-layer BCP device is notably faster, indicating excellent electronic connectivity between the layers. The direct comparison of ~ 1.7 µm thick BCP and NP derived devices exhibit transport rates of $4500\,s^{-1}$ and $2250\,s^{-1}$, respectively, when operated at the maximum power point. We associate the high transport rates k_{trans} to the fact that the presented route allows the formation of exceptionally large TiO_2 nanocrystals within the mesoporous network, while maintaining the block copolymer imposed morphology.[27] Charge recombination rates were significantly reduced in the BCP system with $85\,s^{-1}$, compared to $255\,s^{-1}$ for the corresponding NP devices at the maximum power point (Figure 6). These highly conducting

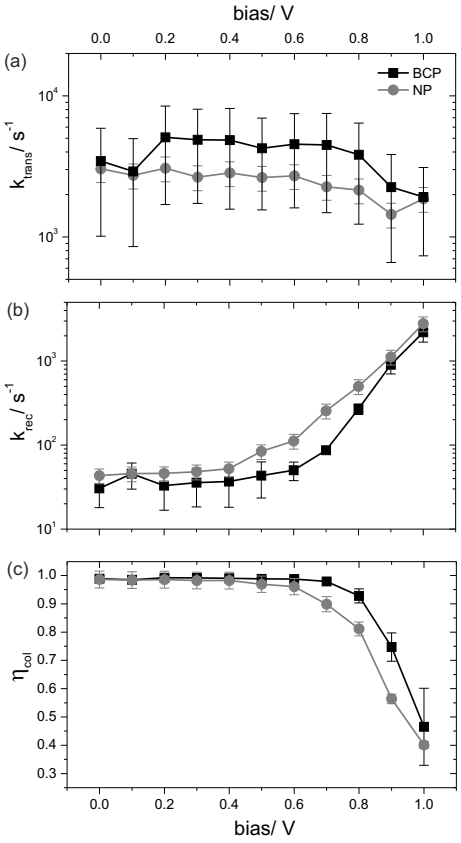

Figure 6. Electronic device characteristics. Direct comparison between block-copolymer assembled photoanodes (BCP, ■) and conventional nanoparticle devices (NP, ●) of similar thickness (1.8 µm). (a) Transport rates (k_{trans}), (b) recombination rates (k_{rec}), and (c) charge carrier collection efficiencies (η_{col}) as a function of the applied bias. While the collection efficiency for standard nanoparticle devices deteriorates above 0.5 V, BCP-derived devices retain high efficiencies close to V_{oc}. The D102 dye was used in all devices.

networks exhibit a somewhat reduced surface area compared to the standard nanoparticle-based photoelectrodes.[27] As the recombination rate k_{rec} is usually linked to the surface-to-volume ratio of the structure, we expect to see enhanced transport rates and lower recombination.[43,44] The bias-dependent charge collection is therefore remarkably different in both systems. For the NP devices, charge collection efficiency (η_{col}) decreases above 0.5 V, while charge collection in BCP devices remains close to unity up to 0.7 V. At $V_{\mathrm{oc}} = 0.9$ V (for the red light used in this measurement), $\eta_{\mathrm{col}} = 0.86$ for the BCP-derived devices compared to $\eta_{\mathrm{col}} = 0.56$ for the NP system. This is consistent with the exceptionally high fill factor of 0.76 obtained with some of these devices.

These results are particularly important since they promise more efficient operation at higher bias, i.e. an enhanced fill factor. In fact, we observe large fill factors (> 0.7) when using the dye D102 up to 2.5 µm in film thickness. Furthermore the open-circuit potential of the BCP-derived devices is above 0.85 V for films thicker than 1.0 µm, which can be explained by the improved transport properties and the narrower distribution of sub-bandgap states (see Supporting Information).

3 Conclusions

In summary, we have demonstrated a straight-forward route for the fabrication of thick mesoporous films with a well defined pore morphology, based on the co-assembly of a high molecular weight block-copolymer and a hydrolytic sol. A study of the time- and temperature-dependent evolution of the shrinkage process of ~ 700 nm thick spin-cast layers enabled the identification of the optimal processing parameters for the layer-by-layer film formation of thick films, avoiding the formation of cracks and delamination. Following a fast, simple and effective annealing protocol, film shrinkage was maximized for each deposition cycle, while preserving the polymer to protect the underlying pores. As a consequence the time and effort to build-up a multilayer stack was drastically reduced. The resulting mesoporous TiO_2 photoanodes exhibited a continuous network with large accessible pores. Increased pore size, film thickness and temperature-stability led to greatly enhanced power conversion efficiencies in solid state dye-sensitized solar cells which are now comparable to the long-optimized nanoparticle system. Significantly enhanced charge transport and charge collection rates at high bias make this system a promising candidate for the increase in the fill factor and open-circuit potential in thick ss-DSCs.

4 Experimental

Substrate preparation. Fluorine doped tin oxide (FTO) coated glass sheets (15 Ohm square^{-1}, Pilkington) were etched with zinc powder and HCl (2 Molar) to obtain the required electrode pattern. The sheets were then washed with soap (2 % Hellmanex in water), de-ionized water, acetone, methanol and finally treated under an oxygen plasma for 10 minutes to remove the last traces of organic residues. The FTO sheets were subsequently coated with a compact layer of TiO_2 (100 nm) by aerosol spray pyrolysis deposition at 450 °C, using air as the carrier gas.
Material fabrication. Block-copolymer derived TiO_2 photoelectrodes were fabricated as follows: poly(isoprene-*block*-ethylene oxide) block-copolymer (PI-*b*-PEO) (0.4 g, molecular weight $M_{\mathrm{n}} = 34.4$ kg mol^{-1}, 28 wt% PEO) was dissolved in an azeotrope solvent mixture (8 ml) of toluene (72.84 w%)

and 1-butanol (27.16 w%). A titanium-containing sol was prepared separately by the addition of titanium(IV) isopropoxide (1.54 ml, Sigma Aldrich, 99.999 % trace metals basis) to hydrochloric acid (0.49 ml, 37 %) under vigorous stirring. 5 min after addition of the titania precursor, the sol was added to the polymer solution and subsequently stirred for a further 30 min. Hybrid films were then deposited from solution by spin coating (1800 rpm, 20 s) or doctor blading. Subsequently the films were exposed to an annealing protocol on a calibrated hotplate (high temperature titanium hotplate, 2000 W with programme regulator, Harry Gestigkeit GmbH), typically for 10 min at 50 °C, followed by a 45 min linear heating ramp to 300 °C and a final dwell time of 5 min at this temperature. The procedure of film deposition and subsequent annealing was repeated several times (typically 3-7 cycles) to achieve the required film thickness. Finally the stack was calcined at 600 °C (3 hours, heat ramp 5 °C min^{-1}, Cole Parmer, EW-33855-35) to remove the organic material and to crystallize the TiO_2. Reference photoelectrodes, based on the standard TiO_2 nanoparticle paste were prepared as follows: NR-18T Dyesol paste (as received) was screen-printed with a T120 mesh over substrates, which were previously coated with a TiO_2 compact layer. The films were subsequently ramped to 500 °within 3 h and held at this temperature for 30 min. Subsequently the hotplate was switched off for the substrates to cool down.

Material characterization. Scanning electron microscopy was carried out on a Leo Ultra 55 with a field emission source at an acceleration voltage of 3 kV. For thermogravimetric analysis samples were characterized with a TA instruments Q500 in high resolution dynamic mode with a ramp of ≈ 2 °C min^{-1}. An Ocean Optics DHL2000 light source with a combined deuterium halogen lamp was used for spectroscopic measurements. A fiber-optic reflection probe (Ocean Optics, R400-7-SR) was used for sample illumination and reflection detection. The reflected signal was detected with an Ocean Optics QE 65000 spectrometer. Optical film thicknesses were then derived by least square fitting of the acquired spectra. Ellipsometric data were taken on a Nanofilm EP3se imaging ellipsometer and the instrument software was used to analyze the data.

Solid state DSC assembly. The mesoporous electrodes were cut down to size and soaked in a 15 mM $TiCl_4$ aqueous bath for 1 hour at 70 °C in an incubator. After rinsing with deionized water and drying in air, the films were heat treated a second time at 500 °C for 45 min in air, then cooled down to 70 °C and finally immersed in a dye solution for 1 hour. The indolene dye used for all the transport measurements was D102, as it was found to be more stable under long time exposure to light in ambient conditions. For the photovoltaic performance measurements, CN04 dye was used.[39] Both dyes where 0.2 mM in a 1:1 volume ratio of tert-butanol and acetonitrile. Spiro-OMeTAD was dissolved in chlorobenzene at varying concentrations ranging from 6 vol% to 15 vol% to optimize pore filling of the substrates of different thicknesses. After fully dissolving the hole transporter, 4-tert-butyl pyridine (tBP) was added with a volume to mass ratio of 1:10 µl mg^{-1} tBP:spiro-OMeTAD. Lithium bis(trifluoromethylsulfonyl)imide salt (Li-TFSI) was pre-dissolved in acetonitrile at 170 mg ml^{-1}, then added to the hole transporter solution at 1:2.4 µl mg^{-1} of Li-TFSI solution:Spiro-OMeTAD. When changing the hole transporter concentration, these two ratios were kept constant. The dyed films were rinsed briefly in acetonitrile and dried in air for 1 minute. Then a small quantity of the hole transporter solution (18-25 µl) was dispensed onto each substrate and left to wet the films for 15 s before spinning at 700 rpm for 45 s in air. The films were left for a minimum period of twenty-four hours in air before placing them in a thermal evaporator where 150 nm thick silver electrodes were deposited through a shadow mask under high vacuum (10^{-6} mbar). The active area of the devices was defined by metal optical masks with 0.09-0.12 cm^2 apertures.

DSC characterization. Solar simulated AM 1.5 sunlight was generated with an ABET solar simulator calibrated to give 100 mW cm^{-2} using an NREL calibrated KG5 filtered silicon reference cell. The $J-V$ curves were recorded with a Keithley 2400 source meter. The Solar cells were masked with a metal aperture defining the active area of the solar cells. The photovoltage decay measurement was performed by a similar method to O'Regan *et al.*[40] as described elsewhere.[41,42]

Acknowledgements

The authors acknowledge Dr. M. Kolle for help with graphics design and Prof. D. Eder for useful discussions. This publication is based on work supported in part by Award No. KUS-C1-018-02, made by King Abdullah University of Science and Technology (KAUST), the EPSRC (EP/F056702/1 and EP/F065884/1), the European Commission (NMP4-SL20010-246123), the Department of Energy (DE-FG02 87ER45298) through the Cornell Fuel Cell Institute (CFCI) and the National Science Foundation (DMR-0605856). M.S. was supported by the Cornell Fuel Cell Institute and the En-

ergy Materials Center at Cornell (EMC2), an Energy Frontier Research Center funded by the U.S. Department of Energy, Office of Science, Office of Basic Energy Sciences under Award Number DE-SC0001086.

[1] B. O'Reagan, M. Grätzel, *N*ature **1991**, *3*53, 737.
[2] J. M. Macak, M. Zlamal, J. Krysa, P. Schmuki, *S*mall **2007**, *3*, 300.
[3] T. Brezesinski, J. Wang, J. Polleux, B. Dunn, S. H. Tolbert, *J.* Am. Chem. Soc. **2009**, *1*31, 1802.
[4] M.E. Franke, T. Koplin, U. Simon, *S*mall **2006**, *2*, 36.
[5] L. D. Bonifacio, D. P. Puzzo, S. Breslav, B. M. Willey, A. McGeer, G. A. Ozin, *A*dv. Mater. **2010**, *2*2, 1351.
[6] T. Brezesinski, D. Fattakhova-Rohlfing, S. Sallard, M. Antonietti, B. M. Smarsly, *S*mall **2006**, *2*, 1203.
[7] S. D., Burnside, V. Shklover, C. Barbé, P. Comte, F. Arendse, K. Brooks, M. Grätzel, *C*hem. Mater. **1998**, *1*0, 2419.
[8] A. Hagfeldt, G. Boschloo, L. C. Sun, L. Kloo, H. Pettersson, *C*hem. Rev. **2010**, *1*10, 6595.
[9] T. Dittrich, E. Lebedev, J. Weidmann, *P*hys. Status Solidi-R **1998**, *1*65, R5.
[10] U. Bach, D. Lupo, P. Comte, J. E. Moser, F. Weissortel, J. Salbeck, H. Spreitzer, M. Grätzel, *N*ature **1998**, *3*95, 583.
[11] H. J. Snaith, *A*dv. Funct. Mater. **2010**, *2*0, 13.
[12] H. J. Snaith, L. Schmidt-Mende, *A*dv. Mater. **2007**, *1*9, 3187.
[13] P. Tiwana, P. Parkinson, M. B. Johnston, H. J. Snaith, L. M. Herz, *J.* Phys. Chem. C **2010**, *1*14, 1365.
[14] L. Schmidt-Mende, M. Grätzel, *T*hin Solid Films **2006**, *5*00, 296.
[15] I.-K. Ding, N. Tétreault, J. Brillet, B. E. Hardin, E. H. Smith, S. J. Rosenthal, F. Sauvage, M. Grätzel, M. D. McGehee, *A*dv. Funct. Mater. **2009**, *1*9, 2431.
[16] M. Law, L. E. Greene, J. C. Johnson, R. Saykally, P.D. Yang, *N*at. Mater. **2005**, *4*, 455.
[17] N. Tétreault, E. Horvath, T. Moehl, J. Brillet, R. Smajda, S. Bungener, N. Cai, P. Wang, S. M. Zakeeruddin, L. Forro, A. Magrez, M. Grätzel, *A*CS Nano **2010**, *4*, 7644.
[18] E. J. W. Crossland, M. Kamperman, M. Nedelcu, C. Ducati, U. Wiesner, D.-M. Smilgies, G. E. S. Toombes, M. A. Hillmyer, S. Ludwigs, U. Steiner, H. J. Snaith, *N*ano Lett. **2009**, *9*, 2807.
[19] M. Nedelcu, J. Lee, E. J. W. Crossland, S. C. Warren, M. C. Orilall, S. Guldin, S. Hüttner, C. Ducati, D. Eder, U. Wiesner, U. Steiner, H. J. Snaith, *S*oft Matter **2009**, *5*, 134.
[20] M. Templin, A. Franck, A. DuChesne, H. Leist, Y.M. Zhang, R. Ulrich, V. Schädler, U. Wiesner, *S*cience **1997**, *2*78, 1795.
[21] D. Y. Zhao, J. L. Feng, Q. S. Huo, N. Melosh, G. H. Fredrickson, B. F. Chmelka, G. D. Stucky, *S*cience **1998**, *2*79, 548.
[22] P. D. Yang, D. Y. Zhao, D. Margolese, D. I. Margolese, B. F. Chmelka, G. D. Stucky, *N*ature **1998**, *3*96, 152.
[23] E. L. Crepaldi, G. J. D. A. Soler-Illia, D. Grosso, F. Cagnol, F. Ribot, C. Sanchez, *J.* Am. Chem. Soc. **2003**, *1*25, 9770.
[24] S. Y. Choi, M. Mamak, N. Coombs, N. Chopra, G. A. Ozin, *A*dv. Funct. Mater. **2004**, *1*4, 335.
[25] B. Smarsly, D. Grosso, T. Brezesinski, N. Pinna, C. Boissiere, M. Antonietti, C. Sanchez, *C*hem. Mater. **2004**, *1*6, 2948.
[26] J. Lee, M. C. Orilall, S. C. Warren, M. Kamperman, F. J DiSalvo, U. Wiesner, *N*at. Mater. **2008**, *7*, 222.
[27] S. Guldin, S. Hüttner, P. Tiwana, M. C. Orilall, B. Ülgüt, M. Stefik, P. Docampo, M. Kolle, G. Divitini, C. Ducati, S. A. T. Redfern, H. J. Snaith, U. Wiesner, D. Eder, U. Steiner, *E*nergy Environ. Sci. **2011**, *4*, 225.
[28] M. Zukalová, A. Zukal, L. Kavan, M. K. Nazeeruddin, P. Liska, M. Grätzel, *N*ano Lett. **2005**, *5*, 1789.
[29] J. Prochazka, L. Kavan, V. Shklover, M. Zukalová, O. Frank, M. Kalbac, A. Zukal, H. Pelouchova, P. Janda, K. Week, M. Klementova, D. Carbone, *C*hem. Mater. **2008**, *2*0, 2985.
[30] N. Krins, M. Faustini, B. Louis, D. Grosso, *C*hem. Mater. **2010**, *2*2, 6218.
[31] W. Chen, X. D. Sun, Q. Cai, D. Weng, H. D. Li, *E*lectrochem. Commun. **2007**, *9*, 382.

[32] S. Agarwala, M. Kevin, A. S. W. Wong, C. K. N. Peh, V. Thavasi, G. W. Ho, *A*CS Appl. Mater. Interfaces **2010**, *2*, 1844.
[33] S. H. Ahn, J. T. Park, J. K. Koh, D. K. Roh, J. H. Kim, *C*hem. Commun. **2011**, *4*7, 5882.
[34] J. Tao, Y. Sun, M. Ge, X. Chen, N. Dai, *A*CS Appl. Mater. Interfaces **2010**, *2*, 265.
[35] M. D. Wei, Y. Konishi, H. S. Zhou, M. Yanagida, H. Sugihara, H. Arakawa, *J.* Mater. Chem. **2006**, *1*6, 1287.
[36] M. Nedelcu, S. Guldin, M. C. Orilall, J. Lee, S. Hüttner, E. J. W. Crossland, S. C. Warren, C. Ducati, P. R. Laity, D. Eder, U. Wiesner, U. Steiner, H. J. Snaith, *J.* Mater. Chem. **2010**, *2*0, 1261.
[37] S. Guldin, M. Kolle, M.Stefik, R. Langford, D. Eder, U. Wiesner, U. Steiner, *A*dv. Mater. **2011**, *2*3, 3664.
[38] G. Floudas, R. Ulrich, and U. Wiesner, *J. Chem. Phys.*, **1999**, *110*, 652.
[39] N. Cai, S.-J. Moon, L. Cevey-Ha, T. Moehl, R. Humphry-Baker, P. Wang, S. M. Zakeeruddin, M. Grätzel, *N*ano Lett. **2011**, *1*1, 1452.
[40] B. O'Reagan, F. Lenzmann, *J.* Phys. Chem. B **2004**, *1*08, 4342.
[41] H. J. Snaith, R. Humphry-Baker, P. Chen, I. Cesar, S. M. Zakeeruddin, , M. Grätzel, *N*anotechnology **2008**, *1*9.
[42] P. Docampo, S. Guldin, M. Stefik, P. Tiwana, M. C. Orilall, S. Hüttner, H. Sai, U. Wiesner, U. Steiner, H. J. Snaith, *A*dv. Funct. Mater. **2010**, *2*0, 1787.
[43] N. Kopidakis, N. R. Neale, K. Zhu, J. van de Lagemaat, A. J. Frank, *A*ppl. Phys. Lett. **2005**, *8*7, 202106.
[44] K. Zhu, N. Kopidakis, N. R. Neale, J. van de Lagemaat, A. J. Frank, *J.* Phys. Chem. B. **2006**, *1*10, 25174.